

See discussions, stats, and author profiles for this publication at: <https://www.researchgate.net/publication/221774731>

Spiral plasmonic nanoantennas as circular polarization transmission filters

Article in *Optics Express* · January 2012

DOI: 10.1364/OE.20.001308 · Source: PubMed

CITATIONS

54

READS

286

6 authors, including:



Kate Bachman

Colorado School of Mines

8 PUBLICATIONS 109 CITATIONS

[SEE PROFILE](#)



Jonathan Peltzer

Colorado School of Mines

3 PUBLICATIONS 74 CITATIONS

[SEE PROFILE](#)



Philip D Flammer

Colorado School of Mines

29 PUBLICATIONS 144 CITATIONS

[SEE PROFILE](#)



Thomas E Furtak

Colorado School of Mines

176 PUBLICATIONS 3,982 CITATIONS

[SEE PROFILE](#)

Some of the authors of this publication are also working on these related projects:



Implementation of Autofocusing Algorithms [View project](#)



Implementation of an Autofocusing Algorithm in a Light Sheet Micro- scope for Imaging Thick 3D Samples [View project](#)

Spiral plasmonic nanoantennas as circular polarization transmission filters

K. A. Bachman,¹ J. J. Peltzer,¹ P. D. Flammer,^{1,*} T. E. Furtak,¹
R. T. Collins,¹ and R. E. Hollingsworth²

¹Department of Physics, Colorado School of Mines, Golden, CO 80401 USA

²ITN Energy Systems, Inc., Littleton, Colorado 80127 USA

*pflammer@mines.edu

Abstract: We present simulation and experimental results for easily fabricated spiral plasmonic antenna analogues providing circular polarization selectivity. One circular polarization state is concentrated and transmitted through a subwavelength aperture, while the opposite circular state is blocked. The spectral bandwidth, efficiency, and extinction ratios are tunable through geometric parameters. Integration of such structures onto a focal plane array in conjunction with linear micropolarizers enables complete Stokes vector imaging, that, until now, has been difficult to achieve. An array of these structures forms a plasmonic metamaterial that exhibits high circular dichroism.

© 2012 Optical Society of America

OCIS codes: (240.6680) Optics at surfaces: Surface plasmons; (050.1220) Diffraction and gratings: Apertures; (110.5405) Imaging systems: Polarimetric imaging; (230.5440) Optical devices: Polarization-selective devices; (160.3918) Materials: Metamaterials.

References and links

1. J. S. Tyo, D. L. Goldstein, D. B. Chenault, and J. A. Shaw, "Review of passive imaging polarimetry for remote sensing applications," *Appl. Opt.* **45**, 5453–5469 (2006), <http://www.opticsinfobase.org/abstract.cfm?URI=ao-45-22-5453>.
2. V. Gruev, J. Van der Spiegel, and N. Engheta, "Dual-tier thin film polymer polarization imaging sensor," *Opt. Express* **18**, 19292–19303 (2010), <http://www.opticsexpress.org/abstract.cfm?URI=OPEX-18-18-19292>.
3. V. Gruev, R. Perkins, and T. York, "CCD polarization imaging sensor with aluminum nanowire optical filters," *Opt. Express* **18**, 19087–19094 (2010), <http://www.opticsexpress.org/abstract.cfm?URI=OPEX-18-18-19087>.
4. J. S. Tyo, B. M. Ratliff, J. K. Boger, W. T. Black, D. L. Bowers, and M. P. Fetrow, "The effects of thermal equilibrium and contrast in LWIR polarimetric images," *Opt. Express* **15**, 15161–15167 (2007), <http://www.opticsexpress.org/abstract.cfm?URI=OPEX-15-23-15161>.
5. Z. Zhao, A. Bermak, F. Boussaid, and V. G. Chigrinov, "Liquid-crystal micropolarimeter array for full Stokes polarization imaging in visible spectrum," *Opt. Express* **18**, 17776–17787 (2010), <http://www.opticsexpress.org/abstract.cfm?URI=OPEX-18-17-17776>.
6. B. Päivänranta, N. Passilly, J. Pietarinen, P. Laakkonen, M. Kuittinen, and J. Tervo, "Low-cost fabrication of form-birefringent quarter-wave plates," *Opt. Express* **16**, 16334–16342 (2008), <http://www.opticsexpress.org/abstract.cfm?URI=OPEX-16-21-16334>.
7. Y. Pang and R. Gordon, "Metal nano-grid reflective wave plate," *Opt. Express* **17**, 2871–2879 (2009), <http://www.opticsinfobase.org/abstract.cfm?URI=oe-17-4-2871>.
8. S.-Y. Hsu, K.-L. Lee, E.-H. Lin, M.-C. Lee, and P.-K. Wei, "Giant birefringence induced by plasmonic nanoslit arrays," *Appl. Phys. Lett.* **95**, 013105 (2009), <http://link.aip.org/link/doi/10.1063/1.3167772>.
9. M. R. Shcherbakov, M. I. Dobynde, T. V. Dolgova, D. P. Tsai, and A. A. Feyanin, "Full Poincaré sphere coverage with plasmonic nanoslit metamaterials at Fano resonance," *Phys. Rev. B* **82**, 193402 (2010), <http://prb.aps.org/abstract/PRB/v82/i19/e193402>.

10. A. C. van Popta, J. Cheng, J. C. Sit, and M. J. Brett, "Birefringence enhancement in annealed TiO₂ thin films," *J. Appl. Phys.* **102**, 013517 (2007), <http://jap.aip.org/resource/1/japiau/v102/i1>.
11. S. L. Wadsworth and G. D. Boreman, "Analysis of throughput for multilayer infrared meanderline waveplates," *Opt. Express* **18**, 13345–13360 (2010), <http://www.opticsexpress.org/abstract.cfm?URI=OPEX-18-13-13345>.
12. L. Feng, Z. Liu, V. Lomakin, and Y. Fainman, "Form birefringence metal and its plasmonic anisotropy," *Appl. Phys. Lett.* **96**, 041112 (2010), <http://apl.aip.org/resource/1/applab/v96/i4>.
13. P. Biagioni, M. Savoini, J.-S. Huang, L. Duò, M. Finazzi, and B. Hecht, "Near-field polarization shaping by a near-resonant plasmonic cross antenna," *Phys. Rev. B* **80**, 153409 (2009), <http://link.aps.org/doi/10.1103/PhysRevB.80.153409>.
14. A. Drezet, C. Genet, and T. W. Ebbesen, "Miniature plasmonic wave plates," *Phys. Rev. Lett.* **101**, 043902 (2008), <http://link.aps.org/doi/10.1103/PhysRevLett.101.043902>.
15. A. Drezet, C. Genet, J.-Y. Laluet and T. W. Ebbesen, "Optical chirality without optical activity: How surface plasmons give a twist to light," *Opt. Express* **16**, 12559–12570 (2008), <http://www.opticsexpress.org/abstract.cfm?URI=OPEX-16-17-12559>.
16. J. K. Gansel, M. Thiel, M. S. Rill, M. Decker, K. Bade, V. Saile, G. von Freymann, S. Linden, and M. Wegener, "Gold helix photonic metamaterial as broadband circular polarizer," *Science* **325**, 1513–1515 (2009), <http://www.sciencemag.org/content/325/5947/1513>.
17. Y. Yu, Z. Yang, S. Li, and M. Zhao, "Higher extinction ratio circular polarizers with heterostructured double-helical metamaterials," *Opt. Express* **19**, 10886–10894 (2011), <http://dx.doi.org/10.1364/OE.19.010886>.
18. W. Chen, Z. Wu, D. C. Abeyasinghe, R. L. Nelson, and Q. Zhan, "Experimental confirmation of miniature spiral plasmonic lens as a circular polarization analyzer," *Nano Lett.* **10**, 2075–2079 (2010), <http://pubs.acs.org/doi/abs/10.1021/nl100340w>.
19. Z. Wu, W. Chen, D. C. Abeyasinghe, R. L. Nelson, and Q. Zhan, "Two-photon fluorescence characterization of spiral plasmonic lenses as circular polarization analyzers," *Opt. Lett.* **35**, 1755–1757 (2010), <http://www.opticsinfobase.org/abstract.cfm?URI=ol-35-11-1755>.
20. A. Kuzyk, R. Schreiber, Z. Fan, G. Pardatscher, E.-M. Roller, A. Högele, F. C. Simmel, A. O. Govorov, T. Liedl, "DNA-based self-assembly of chiral plasmonic nanostructures with tailored optical response," arXiv (2011), <http://arxiv.org/abs/1108.3752v1> [cond-mat.mes-hall].
21. B. Wang, J. Zhou, T. Koschny, M. Kafesaki, and Co. M Soukoulis, "Chiral metamaterials: simulations and experiments," *J. Opt. A: Pure Appl. Opt.* **11**, 114003 (2009), <http://iopscience.iop.org/1464-4258/11/11/114003>.
22. Y. Liu and X. Zhang, "Metamaterials: a new frontier of science and technology," *Chem. Soc. Rev.* **40**, 2494–2507 (2011), <http://dx.doi.org/10.1039/C0CS00184H>.
23. J. J. Peltzer, P. D. Flammer, T. E. Furtak, R. T. Collins, and R. E. Hollingsworth, "Ultra-high extinction ratio micropolarizers using plasmonic lenses," *Opt. Express* **19**, 18072–18079 (2011), <http://www.opticsinfobase.org/oe/abstract.cfm?uri=oe-19-19-18072>.
24. D. J. Hoppe, *Impedance Boundary Conditions In Electromagnetics* (CRC Press, 1995).
25. J. Jin, *The Finite Element Method in Electromagnetics* (Wiley, New York, 2002).
26. P. Flammer, I. Schick, R. Collins, and R. Hollingsworth, "Interference and resonant cavity effects explain enhanced transmission through subwavelength apertures in thin metal films," *Opt. Express* **15**, 7984–7993 (2007), <http://www.opticsinfobase.org/abstract.cfm?URI=oe-15-13-7984>.
27. W. L. Stutzman and G. A. Thiele, *Antenna Theory and Design* (Wiley, New York, 1981).
28. J. Scott Tyo, Charles F. LaCasse, and Bradley M. Ratliff, "Total elimination of sampling errors in polarization imagery obtained with integrated microgrid polarimeters," *Opt. Lett.* **34**, 3187–3189 (2009), <http://www.opticsinfobase.org/abstract.cfm?URI=ol-34-20-3187>.
29. Russell C. Hardie, Daniel A. LeMaster, and Bradley M. Ratliff, "Super-resolution for imagery from integrated microgrid polarimeters," *Opt. Express* **19**, 12937–12960 (2011), <http://www.opticsexpress.org/abstract.cfm?URI=OPEX-19-14-12937>.

1. Introduction

In bulk optics, circular polarization is typically examined using a quarterwave plate in combination with a linear polarizer. Micro-scale or nano-scale polarizing elements are important for a number of applications, for example, imaging polarimetry [1]. Imaging systems using linear micro-polarizing elements have been demonstrated from visible [2,3] to long-wave infrared [4] spectral bands. However, these systems have examined only the linear polarization components of the Stokes vector due to the difficulty in fabricating micropolarizing structures sensitive to circular polarization. One could combine linear polarizing elements with wave plates, but bire-

fringent materials typically used to make quarterwave plates are difficult to fabricate on a micro- or nano-scale. Liquid crystals integrated with metal wire-grid linear polarizers provide one possible approach to obtaining the circular polarization signature for imaging applications [5]. Several alternative approaches for fabricating wave plates have been reported. A dielectric grating with period less than half the operating wavelength acts as a form birefringent material that can be fabricated into a quarterwave plate [6]. These require relatively large aspect ratios along with precise control of the duty cycle and groove depth for quarterwave operation. Subwavelength metal gratings have also been shown to behave as wave plates [7–9]. Dielectric nanorods with a zigzag profile fabricated by off-angle deposition with periodic substrate rotation have been demonstrated as wave plates [10]. Birefringence has been reported in an assortment of antenna analogue and asymmetric plasmonic structures including meanderlines [11], hole arrays [12], cross-shaped antennas [13], and elliptical [14] or single spiral gratings [15] with a central aperture.

An alternative approach would be to use a single structure that transmits right-hand circular polarization while reflecting/absorbing left-hand circular (or vice versa). Chiral materials in nature and synthetic chiral metamaterials have the ability to do this. A gold helix array metamaterial has recently been demonstrated as a circular polarization filter operating in the infrared (3.5–7.5 μm) [16]. Scaling this three-dimensional structure down for operation in the visible will likely be challenging, as will cost-effective manufacturing. Double helices have also been simulated, but are even more difficult to fabricate [17]. Various planar chiral structures have been shown to interact differently with circular polarizations. A single spiral grating in a metal film selectively concentrates one circular polarization state into surface plasmons at the center of the spiral while the alternate circular polarization is concentrated into a donut-shaped region with a dark center [18]. These structures are not transmission structures, and the response has been measured using near-field microscopy or two-photon fluorescence [19]. Therefore, separating left and right polarized signals requires a subwavelength-scale detecting element on top of the metal surface where the light is incident. This makes integration with a detector difficult.

Other exotic structures have been fabricated using a bottom-up approach. DNA-based self-assembled gold nanoparticles have demonstrated circular dichroism in the visible, where, at some wavelengths, one circular polarization is preferred, and, for others, the opposite is preferred by roughly the same amount [20]. This limits its usefulness as a broadband circular polarization filter. Many other interesting chiral structures fabricated by layering two-dimensional structures offset angularly to create helix-like structured metamaterials have been demonstrated and show very interesting properties such as negative indices. See [21, 22] for a review of these structures. However, easily fabricating circularly dichroic metamaterials remains a challenge.

We present simulation and experimental results for a chiral plasmonic structure, inspired by spiral antennas, that demonstrates substantial circular dichroism, passing one circular polarization while blocking the other. In this structure, nested Archimedean spiral gratings in a dielectric-coated metal film couple incident light into surface plasmons directed toward a central aperture. A metal cap over the aperture blocks direct transmission and coincidentally forms a metal-insulator-metal (MIM) waveguide. One circular polarization preferentially transmits through the aperture while the other is trapped in an optical vortex in the structure. This structure is easy to fabricate for visible and NIR (or longer) wavelengths. Fabrication requires only standard thin film processes with three lithography levels having dimensions easily obtained with state-of-the-art photolithography systems. A large-scale array of these structures may form an easily fabricated circular dichroic metamaterial. Alternatively, they may be used individually as circular polarization microfilter elements that can be fabricated simultaneously with ultra-high extinction ratio ($> 10^{11}$) linear structures such as those that we have recently reported [23], providing an economical path to full Stokes vector imaging focal plane arrays.

2. Structure modeling

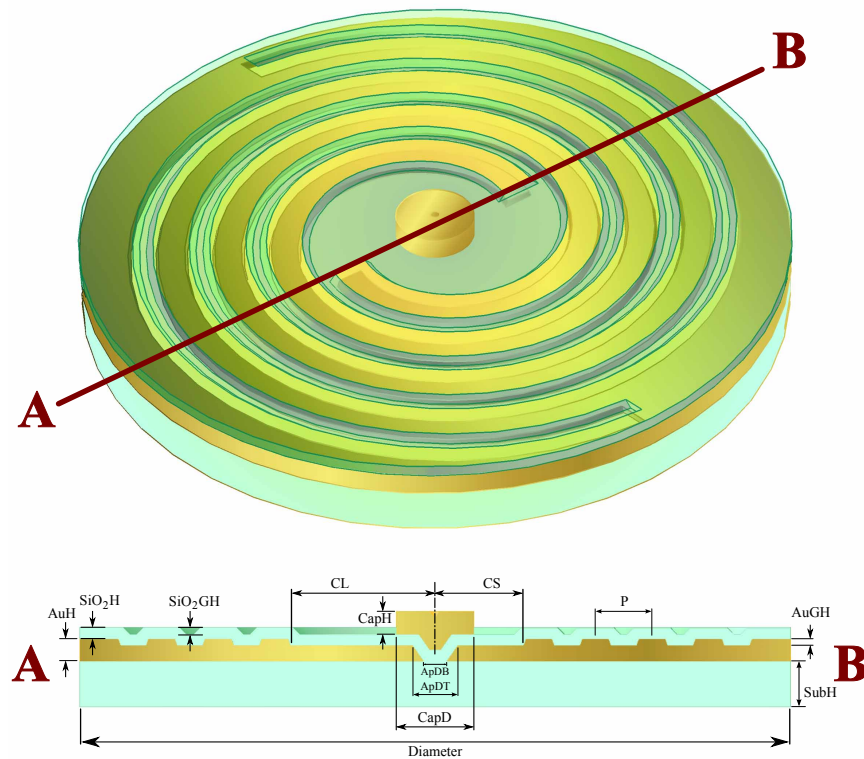


Fig. 1. Cross-section of a model with an Archimedean spiral grating. The structure consists entirely of gold (Au) and silicon dioxide (SiO_2). Unless otherwise stated, the geometric parameters for all the simulations are: the aperture bottom diameter, $\text{apDB}=200\text{nm}$; the aperture top diameter, $\text{ApDT}=400\text{nm}$; the groove height, $\text{AuGH}=60\text{nm}$; the gold thickness where grooves and cavity are cut out, $\text{AuH}=140\text{nm}$; the cap thickness, $\text{CapH}=200\text{nm}$; the cap diameter, $\text{CapD}=688\text{nm}$; the grating period, $P=500\text{nm}$; the cavity length to the nearest groove, $\text{CS}=780\text{nm}$ (note that the cavity can be up to as much as one grating period longer, $\text{CL}=1277\text{nm}$); the deposited SiO_2 thickness, $\text{SiO}_2\text{H}=100\text{nm}$; the SiO_2 groove height, $\text{SiO}_2\text{GH}=100\text{nm}$; the SiO_2 substrate height, $\text{SubH}=400.0\text{nm}$; and the overall diameter, $\text{Diameter}=6280\text{nm}$.

Perspective and cross-sectional views of the structure are shown in Fig. 1. The structure consists entirely of gold (Au) and silicon dioxide (SiO_2). The metal region in the center of the spiral grating is cut out to the same depth as the grooves to form a cavity with a circular aperture in the center. A uniform dielectric layer of SiO_2 covers the entire structure and a metal cap covers the aperture. Sidewall angles and dielectric profiles were chosen to match measurements from fabricated structures discussed below. For Archimedean spirals of fixed periodicity, the arm length is determined by the angular rotation of the arms. For the remainder of the paper, arm length will be given in the angular distance traversed by the arms: 2π is a full rotation, 4π is two rotations for each arm, and so on.

In the simulation, light was normally incident from above (the air side of the structure). Because of memory constraints, an impedance boundary condition [24] at the gold surface

was imposed rather than simulating the fields inside the gold. This type of boundary condition accurately accounts for scattering losses and surface plasmon propagation along the surfaces, but forces direct transmission through the gold to be zero. This is apparent by the lack of the characteristic direct transmission peak near a free-space wavelength of 500nm, near where gold has an interband transition, for films of this thickness. Two-dimensional simulations comparing impedance boundary conditions with full-field simulation inside the metal show only small differences in absolute transmission in the wavelength range of interest with no impact on the qualitative performance [23].

The finite element method with COMSOL Multiphysics simulation software was used for all modeling. A maximum element size of about 66nm was used for the SiO₂, while a maximum element size of about 100nm was used for air. The models were truncated using perfectly matched layers [25], which minimize reflections from the outer edges of the geometry. While these reflections are minimized, in three dimensions, some small oscillations in our simulated transmission may be introduced due to residual reflections from the outer boundary of the model. Memory constraints limited the size of simulations, limiting the spiral arm lengths to an angular distance of 4.5π .

Figure 2 shows field plots for one model at the 700nm free-space wavelength for left-circular (LC) (a, c, and e) and right-circular (RC) (b, d, and f) light. Figure 2(a)-(d) show the time-averaged power flow (Poynting vector), and Fig. 2(e) and (f) each show a snapshot of the z-component of the electric field. We are using the convention that right-circular means that, in a plane perpendicular to the propagation, looking in the direction of propagation, the electric field rotates in the clockwise direction. Our spiral configuration effectively concentrates RC polarized light into the MIM waveguide created by the cap and then transports the energy out of the aperture. The field created in the aperture is essentially a rotating dipole that effectively radiates out of the aperture and into the far-field. For LC polarized light, the field is concentrated into a plasmonic vortex that circulates around the cap on the top metal surface and in the MIM waveguide until the power is absorbed due to ohmic losses. Therefore, this polarization does not effectively radiate. The time-harmonic animations of the electric field (See the media links in the figure caption.) clearly show the rotating dipole for RC and the multipolar field vortex for LC. Interestingly, the grating efficiently couples both polarizations into the central cavity, where the magnitude of the Poynting vector for both exceeds 50 times the incident magnitude.

The time-averaged power flow (Poynting vector) was integrated just below the aperture to yield the magnitude of the power exiting the structure. Representative results are given in Fig. 3 and Table 1. For the models shown in Fig. 3(a), the effect of changing the spiral arm length is shown in Fig. 3(b). All of the simulations showed a preference for RC transmission over LC. Note that inverting the handedness (the angular direction of increasing radius) would result in an LC-selecting element [15]. As the spiral arm length increases, the grating more effectively couples RC light into the plasmon, increasing the transmission through the aperture and narrowing the bandwidth, which is expected for grating-coupled devices. For the different model arm lengths varying from 1.425π to 4.5π , the relative transmission integrated over all wavelengths increased from 31.3 to 80.1 times the incident power. For comparison, we modeled a bare aperture in gold with no grating, cap, or SiO₂ coating, also plotted in Fig. 3(b). Comparing the transmission with that of the structures with spiral gratings demonstrates a strong transmission enhancement that is characteristic of coupling gratings with subwavelength apertures in metal films [26]. While the absolute transmission increases as the number of turns increases, the active area efficiency (transmission normalized to the spiral area) actually decreases because the area of the structure increases faster than the transmission. Referring to Table 1, the active area efficiency decreased with increasing arm length, from 13.70% to 8.62%. Decreasing efficiency with increased arm length (number of grating grooves) is consistent with results for

linear structures [23].

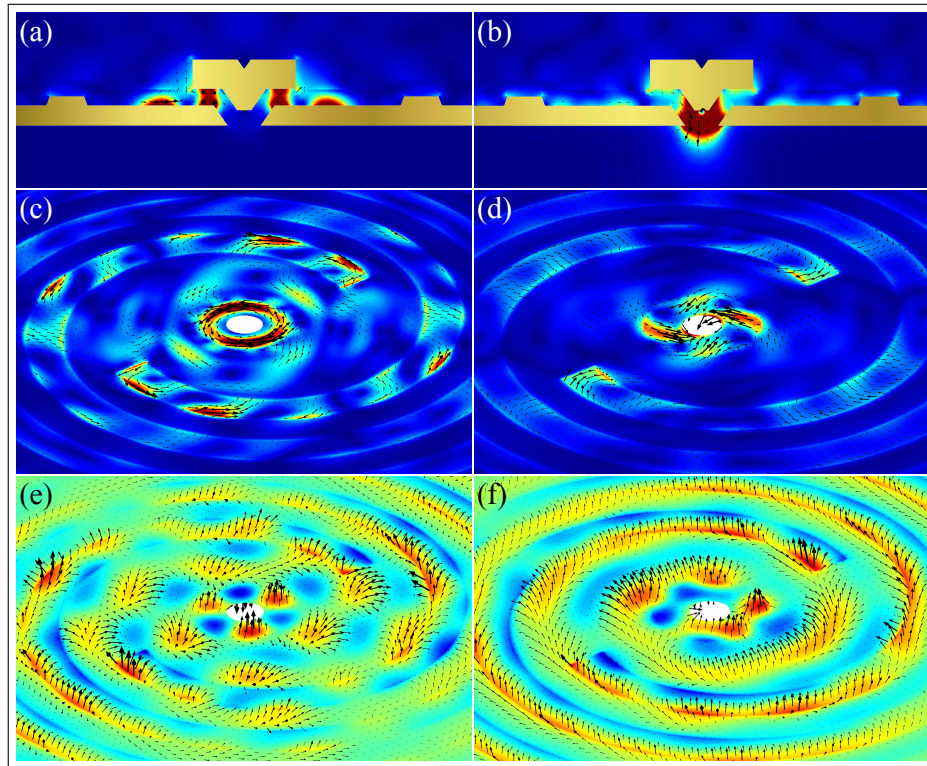


Fig. 2. Vertical and horizontal cross-sectional time-averaged power flow (a-d) and electric field (e,f) snapshots of a 4.2π -turn model irradiated with 700nm left-circularly (a, c, e) and right-circularly (b, d, f) polarized light. For e, (click [Media 1](#) for animation) and f, (click [Media 2](#) for animation), the surface is the z -component of the electric field (which represents plasmons traveling parallel to the metal surface), while the arrows show the direction and magnitude of the electric field, and the colors range from dark blue for ≤ 10 to dark red for ≥ 10 normalized to the incident electric field. For the power flow plots, colors range from dark blue for 0 to dark red for ≥ 50 normalized to the magnitude of the incident Poynting vector. Vertical cuts are taken through the center of the aperture, while horizontal cuts are taken 10nm above the grating ridges.

The LC transmission remains roughly constant with increasing arm length, leading to increased circular polarization selectivity with increasing arm length. Peak extinction ratios may not be representative of actual performance because they are dominated by a local minimum at 700nm in the LC transmission, so we present the wavelength integrated (power out of the aperture for preferred polarization divided by the power transmitted by the unwanted polarization) values in Table 1. The extinction ratios varied from 2.14 to 6.49 with the longest arm length showing a slightly lower extinction ratio than its predecessor due to slightly higher LC transmission for that arm length. The power out of the aperture for the 4.2π model with RC, LC, and linearly polarized light (x -direction, XL, and y -direction, YL) is shown in Fig. 3(c). The results show that the XL and YL response is about 28% of that for RC, with the LC response generally less than that for both XL and YL.

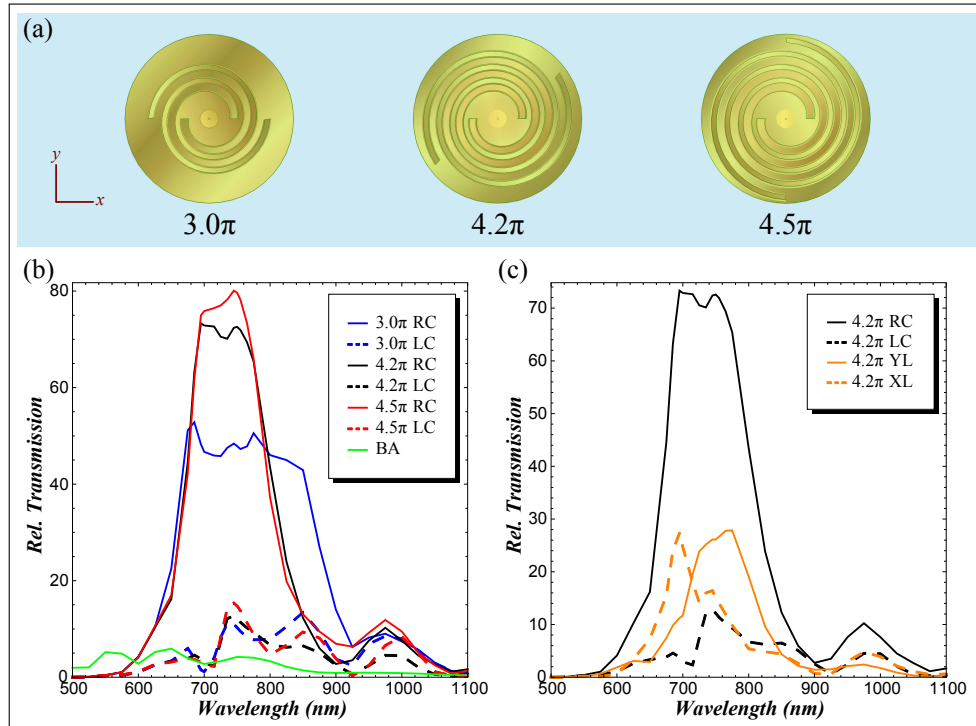


Fig. 3. Simulation results. (a) Modeled geometries. Plots (b) and (c) show relative transmission normalized to the power incident on the aperture: (b) Spiral arm length study; (c) Comparison of right- and left-circular, and linear (x- and y-directions) polarization results.

Table 1. Simulation results summary

Model	Polarization	Spiral Dia. (nm)	Relative Trans. (RC)	Wavelength of RC Peak (nm)	Extinction Ratio (RC/LC)	Active Area Efficiency RC (%)
1.425π	circular	3025	31.3	725	2.14	13.70
3.000π	circular	4595	52.8	685	4.67	10.00
4.200π	circular	5798	73.3	695	6.49	8.72
4.500π	circular	6095	80.1	745	5.77	8.62
bare aperture	circular	0	5.9	650	1.00	–
4.200π	circular	5798	73.3	695	6.49	8.72
4.200π	linear (X)	5798	27.3	695	–	3.25
4.200π	linear (Y)	5798	27.9	775	–	3.31

Another property of the structure is how different incident polarization states are transformed when transmitted. Interestingly, all incident polarization states are transmitted as predominantly LC polarized light. This is especially interesting given that the structure blocks incident LC polarized light. This is evident from the time-harmonic animation for the RC-incident light where the rotating dipole, discussed above, rotates counter-clockwise rather than clockwise (see the media link in the caption of Fig. 2). Animations for the linear polarization states, and animations on the output side of the structure (not shown), demonstrate the same effect: LC, RC, XL, and YL all transmit predominantly LC polarized light. In terms of a bulk optics analog, this

is the same behavior observed for a stack consisting of a quarterwave plate, linear polarizer, and another quarterwave plate, where the two fast axes of the quarterwave plates are parallel, and the linear polarizer is rotated 45 degrees with respect to the fast axes. Keeping the orientations of the wave plates and linear polarizer fixed, one circular polarization (say LC) is blocked: in the first wave plate, it is transformed into a linear polarization perpendicular to the linear polarizer, and thus blocked. The other circular polarization (RC) is passed: it is transformed by the first wave plate into a linear polarization parallel to the linear polarizer; then the second wave plate transforms the now linear polarization state to the opposite circular polarization (LC). Incident linear polarizations are transformed into circular polarization by the first quarterwave plate, then half the light for both cases is passed by the linear polarizer; after passing through the linear polarizer, the polarization state is linear, the same as for RC, but with lower amplitude than the RC incident light, so the output polarization state will also be LC. This is exactly the behavior predicted for our structure, and, where, in bulk optics, this complicated stack of optics is required, our single compact plasmonic microstructure performs the same transformation.

For broadband applications, we simulated a logarithmic spiral, a common radio frequency antenna structure [27] with roughly the same footprint as the 4.5π model. An integrated extinction ratio of 6.27 and broadband RC peak with peak width of about 400nm (from 650nm to 1050nm) were obtained. The peak transmission was approximately 46 relative to the power incident on the aperture area, and the transmission efficiency normalized to the structure footprint was 4.9%.

3. Experimental verification

The arrays of devices used for the experimental demonstration were fabricated on polished microscope slides coated with a 200nm layer of gold on top of a 2.5nm titanium adhesion layer. All patterning was done by electron beam lithography in a JEOL 840 scanning electron microscope with NPGS software. We note that, while e-beam lithography was used, the dimensions are within the range of modern optical lithography. In the first patterning level, 4×4 arrays of circular apertures and alignment marks were defined in the positive resist PMMA (polymethylmethacrylate) and cut completely through the metal using broad beam argon ion milling. In the second patterning level, spiral gratings and the central cavity were defined in PMMA and cut partially into the gold surface using argon ion milling. For the samples reported here, the groove and cavity depth were approximately 60nm with spiral arm length (5 values from 2 to 6π turns) and cavity width (4 values from 500 to 1000nm radius) as variable parameters. This was followed by blanket deposition of 100nm SiO_2 using plasma enhanced chemical vapor deposition. In the final patterning level, a metal cap was fabricated over the aperture using a lift-off process. The alignment marks were also covered at this processing level to minimize the transmission of unfiltered light. Geometrical parameters (grating period, cavity width, aperture width and position, cap width and position) of the fabricated structures were measured using scanning electron microscopy.

Experimental far-field spectra were collected using an optical microscope configured for transmission measurements coupled to an Acton 300i spectrometer with a Princeton Instruments Spec-10:100BR liquid nitrogen cooled silicon CCD array detector. A fiber-coupled tungsten halogen lamp provided white light for an input arm which included divergence control lenses and a polarization control stack consisting of zero-order quarter- and half-wave plates in conjunction with a linear polarizer that could change the input polarization to any controlled polarization state. Light was incident on the air side of the structure and collected with a long working distance objective (N.A. = 0.5) after transmission through the spiral structures and 1mm thick glass substrate. The approximately $24\mu\text{m}$ collection spot size was smaller than the 4×4 array size. The collected light was focused onto the end of an optical fiber positioned in a

conjugate relationship to the sample plane. The opposite end of the fiber was optically coupled to the entrance slit of the spectrometer. Raw spectra were background subtracted and normalized to a white light measurement made with no sample in place to give absolute transmission. However, no correction for the finite collection angle of the objective was made.

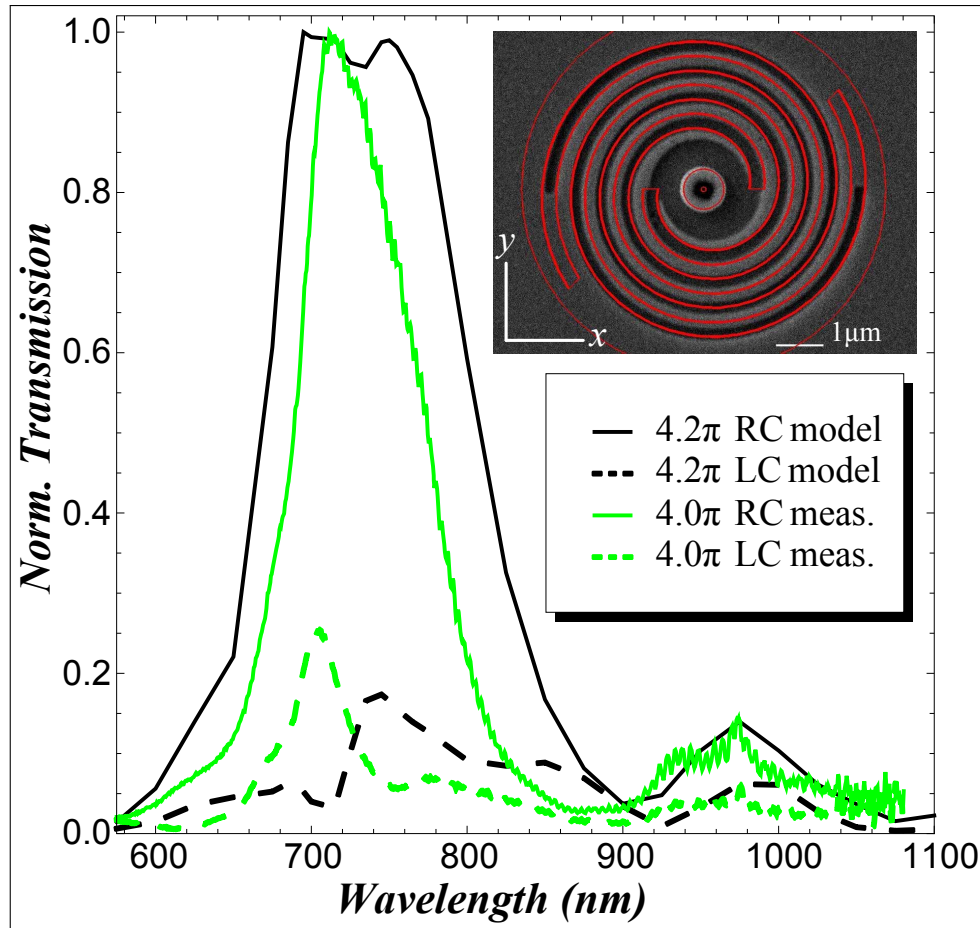


Fig. 4. Experimental and simulated transmission data compared. The simulations and measurements are separately normalized to the RC maximum. The inset shows an overlay of the model geometry on an SEM image of the measured structure.

Figure 4 compares the 4.2π simulation and the far-field transmission measurement for the fabricated structures having the closest geometric match. Good agreement is obtained for RC polarization between the main peak around 700nm as well as a secondary peak around 975nm. The measured main peak width is smaller than the simulation, possibly because of the geometric differences between the model and fabricated structure. An overlay of the 4.2π model spiral geometry on the SEM image of the measured structure is shown in the inset, providing a visual representation of the geometric differences. Smaller measured peak widths are also seen in comparing structures with 3π -turn spirals. For LC polarization, the 4π measurement and simulation have similar amplitudes but different peak locations. The integrated right/left circular extinction ratio was 5.1 for the measurement, reasonably close to the value of 6.49 predicted by

the model.

Structures beyond those simulated were fabricated to experimentally study the effects of cavity width. Measurements of structures with different cavity widths (not shown in the figures) indicate that peak position and amplitude for LC polarization depend strongly on cavity width, while the RC transmission is little affected. This leads us to attribute the LC differences between experiment and model to geometric differences such as cavity width. Experimentally, for fabricated 4π structures, the right/left extinction ratio generally decreased with increasing cavity width. The shortest cavity width had an integrated extinction ratio of 8.3, which decreased to 5.1 for longer fabricated cavity widths.

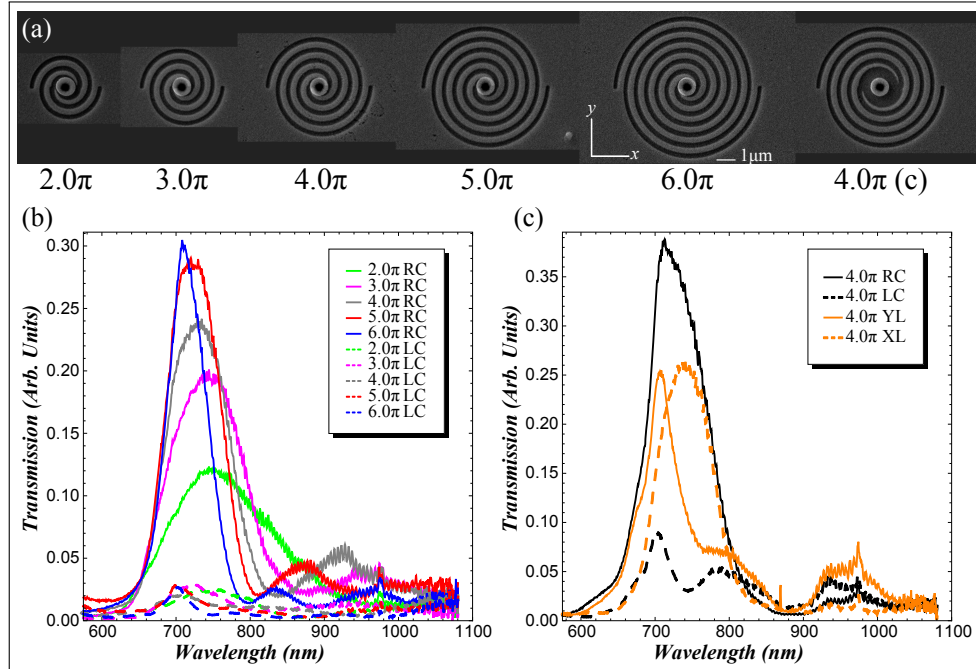


Fig. 5. Experimental results. (a) Structures measured in (b) and (c). Plots (b) and (c) show relative transmission as a function of free-space wavelength (nm): (b) Spiral arm length study; (c) Comparison of right- and left-circular, and linear (x- and y-directions) irradiation results.

SEM images of several fabricated structures, scaled to show relative size, are shown in Fig. 5(a). Figure 5(b) shows the experimental transmission curves for structures with the smallest cavity width (highest integrated extinction ratio) and various arm lengths. The RC peak blue-shifts and line width shrinks monotonically as the arm length increases, behavior that is generally predicted by our simulations. The integrated right/left extinction ratio increases monotonically from 5.9 to 11.3 as arm length increases. Figure 5(c) provides circular and linear polarization measurements comparable to the simulation results of Fig. 3(c). Peak shapes for the two linear polarizations are quite similar between the measurement and simulation, but the orientations are switched with the shortest wavelength peak occurring for polarization along the x-axis for the simulation and along the y-axis for the measurement. This can be directly attributed to geometric differences because the peak response for linear polarization will be a function of the cavity width. Maximum cavity width occurs along the y-axis for the simulation.

However, maximum cavity width occurs along the x-axis for the fabricated structure because the fabricated arms stop short of the x-axis as can be seen by close examination of the inset to Fig. 4.

Applications for the structures described here are extensive. A large array of these structures may be used to form an easily fabricated circular dichroic metamaterial (Fig. 6(a)). Such a metamaterial could be used as a VLSI-compatible circular-dichroic thin film filter, which is currently achieved using a quarterwave plate/linear polarizer combination.

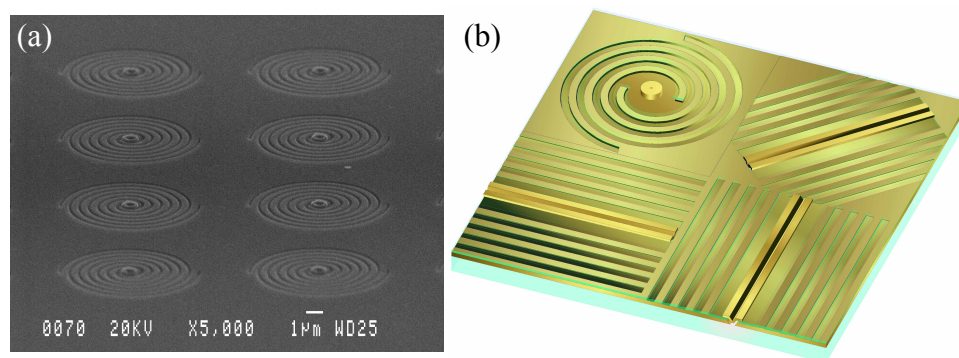


Fig. 6. (a) Array of structures to form a circular dichroic metamaterial, and (b) illustration of a full Stokes polarization superpixel.

The structure may also be used individually as circular micropolarizers that can be fabricated simultaneously with ultra-high extinction ratio ($> 10^{11}$) linear structures such as those that we have recently reported [23] to form a 4-pixel polarization superpixel. Advances in nanofabrication have led to increased attention to division of focal plane systems into superpixels, where an array of micropolarizing elements is monolithically integrated directly on a focal plane array sensor. The mechanical robustness, permanent polarizer-to-sensor alignment, and potential for low-cost fabrication provide significant advantages for this approach, while recent advances in image reconstruction algorithms mitigate the artifacts that arise from each pixel looking at a slightly different part of the scene [28,29]. This new superpixel provides an economical path to full Stokes vector imaging focal plane arrays (Fig. 6(b)). The fact that the central peak transmission wavelength is determined by the grating periodicity of the structures gives us the ability to very easily change the transmission band to any wavelength where the metal supports plasmons. For shorter wavelengths, a metal such as silver must be used, but the fabrication method will remain the same, and the length scales are well within reach of state-of-the-art VLSI fabrication techniques. Because only the lateral dimension must change, the same lithography steps may be used to fabricate an array of filters for different circular and linear polarizations and different colors as well, allowing for combination polarization/color superpixels to be fabricated simultaneously. Any combination of polarization state and color measurement may be chosen to fit the needs of the application.

4. Conclusion

Simulation and experimental results are presented for chiral circular micropolarizing transmission structures. The structures feature nested Archimedean spiral gratings similar to longer wavelength antenna designs. Simulations and experiment agree quite well. The structures provide controllable bandwidth and peak wavelength. Fabrication requires only standard thin film

processes with three lithography levels having dimensions easily obtained with state-of-the-art photolithography systems. These structures offer the possibility of single-element circular polarization transmission microfilters that can be combined with linear transmission microfilters on focal plane arrays to enable full Stokes vector polarization imaging. They may also be used in a large array to form a circular dichroic metamaterial.

Acknowledgments

This work was sponsored by the Air Force Office of Scientific Research under contract number FA9550-10-C-0024. We acknowledge fabrication assistance from Greg Nuebel and Tim Rea.